Revision 1 Word Count: 9210

Solving the iron quantification problem in low-kV EPMA: An essential step toward improved analytical spatial resolution in electron probe microanalysis—Fe-Sulfides

Aurélien Moy[1]*, Anette von der Handt[2] and John Fournelle[1]

[1.] Department of Geoscience, University of Wisconsin, Madison, WI 53706, USA.

[2.] Department of Earth Sciences, University of Minnesota, Minneapolis, MN 55455, USA.

* Corresponding author: amoy6@wisc.edu

Abstract

The use of the field emission gun in scanning electron microscopy permits the imaging of sub-micrometer-size features. However, achieving sub-micrometer analytical spatial resolution in electron probe microanalysis (EPMA) requires both reducing the electron beam size and reducing the accelerating voltage to achieve the desired sub-micrometer interaction volume. The resulting quantification of the first-row transition metals at low accelerating voltage, i.e., below 7-8 kV, is problematic as the main characteristic X-ray lines (Kα) cannot be excited at these conditions. Furthermore, the use of the Lα and Lβ soft X-ray lines for quantification is complicated by bonding and self-absorption effects resulting in not-yet determined mass absorption coefficients and hence in the failure of the traditional matrix correction procedure. We propose two methods to circumvent these low kV analysis limitations: using the non-traditional Fe Lℓ line, and using universal calibration curves for the more traditional Fe Lα and Lβ lines. These methods were successfully

This is the peer-reviewed, final accepted version for American Mineralogist, published by the Mineralogical Society of America.
The published version is subject to change. Cite as Authors (Year) Title. American Mineralogist, in press.
DOI: https://doi.org/10.2138/am-2022-8027. http://www.minsocam.org/

applied to Fe-sulfide minerals showing accurate quantification results by EPMA at reduced kV, necessary for accurate quantification of sub-micrometer sulfide grains.

Keywords: EPMA, sulfides, low-kV, iron, microprobe, SXES, EMPA, X-ray

Introduction

Electron probe microanalysis (EPMA) is a characterization technique that is routinely used for qualitative and quantitative analysis of micrometer-sized volumes. The technique has seen many significant advances in the last decades (Llovet et al. 2020). One of them has been developing and integrating Schottky field emission guns (FEGs) in microprobe instruments. These types of electron sources produce a stable, bright and narrow electron beam, resulting in a smaller beam diameter compared to tungsten and LaB_6 sources and hence offer a significant increase of the spatial imaging resolution. However, to better use this resolution improvement for quantitative purposes, it is also essential that the electron beam energy is reduced, typically from the traditional 15 or 20 kV to 7-8 kV or less. The combination of reduced beam size through the availability of FEGs and reduced electron interaction volume through using lower beam energy then permits the possible successful analysis and quantification of sub-micrometer features.

Figure 1 illustrates this for the Fe Kα and Lα X-ray production volume diameters in FeS_2, using the Monte Carlo code PENEPMA/PENELOPE (Llovet and Salvat 2017; Salvat 2019). By decreasing the accelerating voltage from 20 kV to 7 kV (assuming an electron beam diameter of 80 nm), the diameter of the contour delimiting an area where 99% of the considered X-rays are produced, is reduced from 3 μm to about 0.75 μm, as shown on Figure 1. Hence, the analytical spatial resolution is increased by a factor of 4. Reducing the beam diameter will only reduce the X-ray production volume's diameter by the same amount, therefore not drastically improving the

47 analytical resolution. The critical parameter governing the analytical spatial resolution is the
48 accelerating voltage. It is worth noting that at 10 and 20 kV, the diameter of the X-ray production
49 volume for the Fe Kα and Fe Lα X-ray lines are similar, as summarized in Table 1 . However, at
50 7 kV the maximum of the produced X-ray intensity for the Fe Lα X-ray line is about three times
51 higher than the maximum of the produced X-ray intensity for Fe Kα X-ray line at 10 kV.

52 We are not, however, the first to investigate the use of low kV EPMA for sulfides. Desborough et
53 al. (1971) ran a successful series of experiments, measuring S Kα at 6 kV on the USGS ARL
54 EMX electron probe. The goal was not improving the analytical spatial resolution but rather that
55 of effectively eliminating matrix effects. Using a suite of synthetic in-house sulfide reference
56 materials (Czamanske and Ingamells, 1970), they concluded that "a linear calibration curve
57 relating X-ray intensity to sulfur concentration eliminates the need for using complex computer
58 corrections required at higher operating voltages" – recall the state of computing five decades
59 ago.

60 **Difficulties of EPMA at low accelerating voltage**

61 Two[1] methods can be distinguished to improve the analytical spatial resolution in EPMA (and as
62 demonstrated by Desborough et al. (1971), reduce the magnitude of the matrix correction for some
63 elements): low overvoltage, and low voltage. The low overvoltage approach employs lowering the
64 accelerating voltage, or electron beam energy, to just above the ionization energy required to

[1] There is a third possible method, if special sample preparation is utilized. Kubo et al. (2013) thinned a specimen using focused ion beam (FIB) technology and with a 30 kV electron beam achieved high spatial resolution EPMA results in a semi-conductor specimen.

produce the X-ray transition of interest (i.e., low overvoltage) such as 8-10 kV for the Fe Kα X-ray line. The beam electrons have enough energy to produce the ionization only in a very small volume near the landing point of the electron beam, resulting in high analytical spatial resolution, as shown on Figure 1c. One disadvantage of this method is that the X-ray count rates will also drop as the probability of producing the desired ionization is reduced when the electron energy gets closer to the ionization edge threshold. This is further compounded because less electrons will contribute to the production of the desired ionization and, due to other interaction mechanisms, will quickly bring the electron energy below the required ionization energy threshold.

The second analytical approach consists of reducing the accelerating voltage to a low absolute value, e.g., 7 kV instead of the conventional 15 kV or 20 kV. The primary electrons have fewer energy and thus travel, on average, shorter distances before losing too much energy and contributing to the production of the specific X-ray line. Therefore, the electron interaction volume is consequently reduced, constraining the production of the characteristic X-rays of interest within a much smaller volume. Going much lower in kV is counterproductive, as the electron beam tends to widen on some FEG instruments (Pinard and Richter 2014) and the count rates tend to decrease rapidly. Increasing the beam current can compensate for the lowered count rates but aggravates the increase in beam diameter.

However, three main issues arise when considering operating at low accelerating voltage: (1) X-ray lines conventionally used at high kV may not be excited at low kV. The Kα X-ray line of the first row transition elements cannot be excited for accelerating voltages below 5-8 kV. The same situation happens for some of the rare earth elements where the Lα X-ray line cannot be excited at such low accelerating voltages. For example, the element Fe whose critical excitation energy for the production of the Fe Kα X-ray line is 7.114 keV (Zschornack 2007) cannot be excited with

88 electron beam energies lower than this threshold. (2) The measurements will be more sensitive to
89 the state of the sample surface because the electrons no longer penetrate deeply into the material.
90 Hence, for both the unknown specimen and the standards, the quality of surface polish, the surface
91 fidelity and cleanliness, and the conductive coating thickness will be critical to achieve accurate
92 measurements. In particular, for maximum accuracy, the accurate determination of the coating
93 thickness should be performed to account for thickness variations between the unknown and the
94 standards. Coating unknowns and standards simultaneously can help minimize the difference in
95 coating thicknesses. However, this may not be sufficient depending on the geometry of the coater.
96 Rotating the samples during the coating process may be needed to homogenize the coating
97 thickness between samples. At low accelerating voltages, these variations, resulting in differences
98 in X-ray production and absorption, will be more pronounced. And (3), since the primary electrons
99 no longer penetrate as deep or spread out radially as much, they deposit their energy in a very small
100 volume and may lead to sample damage. These problems encountered at low kV are discussed in
101 detail in several recent publications (Jercinovic et al. 2012; Gopon et al. 2013; Kearns et al. 2014;
102 Saunders et al. 2014; Buse and Kearns 2015, 2018; Moy et al. 2019a, 2019b).

103 In the present work, Fe-sulfide minerals were studied because of their importance in geoscience
104 and materials science in numerous ways. For example, the analyses of the Fe–S–As minerals in
105 gold deposits can illuminate the deposition mechanism of Au in sulfides, to better understand and
106 to improve the ore formation models (Zhang et al. 2014). The study of sulfides is also used to
107 understand the formation and the evolution of our solar system. The composition and crystal
108 structure of sulfide inclusions found in chondrites and as fine-grained rims, with the help of Fe-Ni-
109 S isothermal phase diagrams, can be used to constrain oxygen fugacity and cooling history of such
110 objects and illuminate the processes and conditions of chondrite petrogenesis (Harries and

Langenhorst 2013; Schrader et al. 2015; Schrader and Zega 2018). The study of sulfide inclusions is also relevant in the determination of origins of deep Earth diamonds (Deines and Harris 1995). Characterization of sulfide inclusions in steels is also of great importance because these inclusions can create numerous problems such as breakage of steel wires during drawing, fatigue failure or surface flaws.

We focus here on the study of the transition element iron in iron-sulfide minerals at low accelerating voltage. At low accelerating voltages (7 kV and below) the traditionally used characteristic K X-ray lines of iron will not be excited, and thus our study considers the use of the Lα (L_3-$M_{4,5}$ electron transition) and Lβ_1 (L_2-M_4 electron transition) X-ray lines to perform quantification by EPMA, using the Fe Lα+Lβ_1 area k-ratio (i.e., the area of the Lα and Lβ_1 X-ray lines measured on the unknown and divided by the area measured on a standard) associated to a calibration curve (Moy et al. 2019a; 2019b). Note that for the sake of simplicity the Lβ_1 transition will be denoted Lβ in the rest of the text. We also investigate the possibility of using the Fe Lℓ (L_3-M_1 electron transition) X-ray line for quantification.

Materials and Methods

EPMA measurements were performed using a CAMECA SXFive-FE instrument located at the Eugene Cameron electron microscopy laboratory, Department of Geoscience, University of Wisconsin-Madison and using a JEOL JXA-8530FPlus instrument at the Department of Earth Sciences, University of Minnesota. Both electron microprobes are equipped with field emission electron guns and use the Probe for EPMA software to operate the instrument and to acquire the data (Donovan et al. 2021). Additionally, the resulting calibration curve was validated on a separate instrument, a CAMECA SX51 at UW Madison Department of Geoscience.

Fe-sulfides Samples

A total of 14 Fe-sulfides of known composition were used in this study: 11 Fe-sulfide standards were used for the measurements performed with the SXFive-FE instrument and 12 Fe-sulfides standards were analyzed with the JXA-8530FPlus. The iron elemental concentrations in these sulfides range from 5.79 wt% up to 63.53 wt%. On both instruments, a pure Fe-metal sample was used as a standard. The samples' Fe concentrations as well as their sources are given in Table 2.

The Fe-sulfide standards were initially precisely characterized by EPMA at 15 kV (20 kV for the arsenopyrite standard) and 20 nA with PHA in wide differential mode using the SXFive-FE instrument. At these conditions, traditional Kα X-ray lines were used for all the elements except for Sn where the Lα line was used instead (which is considered as a main characteristic X-ray line for this element). A minimum of 5 points were measured on different locations, and the PAP matrix correction algorithm (Pouchou and Pichoir 1991) with the MAC30 mass absorption coefficients (Heinrich 1987) was employed to determine the elemental composition of the different specimens. For each sample, the S Kα X-ray line position was re-determined by a peak scan to avoid any peak shift error. The measured compositions are given in Table 2. Some of the minerals used were synthesized by Czamanske at the USGS in the late 1960s (Czamanske and Ingamells 1970). The slightly low total of the synthetic Zn-Fe-S samples Czamanske37 and Czamanske35 can be partially attributed to the fact that these samples are composed of small grains (~5 μm diameter); hence, there is a lack of characteristic X-rays produced by secondary fluorescence in the grains, leading to a deficit of the total produced X-rays, compared to a bulk sample of the same material ("size effect": Fournelle 2006). This deficit of characteristic X-rays can easily account for an underestimation of the Fe concentration of 1 wt% in these small grains, where the pure Fe standard

This is the peer-reviewed, final accepted version for American Mineralogist, published by the Mineralogical Society of America.
The published version is subject to change. Cite as Authors (Year) Title. American Mineralogist, in press.
DOI: https://doi.org/10.2138/am-2022-8027. http://www.minsocam.org/

used was significantly larger in size. The measured iron compositions were used in the following work.

Spectra acquisition

Three analytical sessions using an accelerating voltage of 7 kV were performed with the SXFive-FE microprobe to acquire the Fe Lα and Lβ spectra, as well as the Fe Lℓ spectrum, on the different samples. During the first session, spectra from the following samples were recorded: Fe metal, pyrite, stannite, pentlandite, pyrrhotite, chalcopyrite, bornite and cobaltite. During the second session of measurements, the following new samples were analyzed, as well as samples previously analyzed in order to verify the reproducibility of the measurements: Canyon Diablo troilite, CZ4 FeS, Mnt8 FeS, pyrrhotite, pyrite and Fe metal. The third session consisted of the measurement of the arsenopyrite and Fe metal specimens. With the JXA-8530FPlus microprobe, two analytical sessions were also performed at 7 kV to record the Fe spectra. During the first session, the same samples as the ones analyzed during the first session on the SXFive-FE instrument were measured at 7 kV and 20 nA: Fe metal, pyrite, stannite, pentlandite, pyrrhotite, chalcopyrite, bornite and cobaltite, while for the second session, the following samples were measured at 7 kV and 50 nA: chalcopyrite, Czamanske37 ZnFeS, Czamanske35 ZnFeS, chalcocite, Canyon Diablo troilite and pure Fe.

Three wavelength-dispersive spectrometers (WDSs) were employed on the SXFive-FE instrument using LTAP (2d = 25.745 Å), TAP (2d = 25.745 Å) and PC0 (2d = 45.0 Å) diffractor crystals with a takeoff angle of 40°. A Thermo Scientific UltraDry energy-dispersive spectrometer (EDS) was also used on that instrument to record the spectra, also at a 40° takeoff angle. With the JXA-8530FPlus instrument a different type of spectrometer was used to record the X-ray spectra: a Soft X-ray Spectrometer (SXES, JEOL Inc.) consisting of an extended range diffraction grating JS2000,

and a Peltier-cooled CCD camera (Terauchi et al. 2010). The SXES spectrometer records the whole X-ray spectrum between 240 and 2800 eV simultaneously (similar to a SiLi or SDD energy dispersive spectrometer but with a spectral resolution similar to WDS-TAP). This spectrometer also has a takeoff angle of 40°. The electron beam conditions were set to 7 kV and 90 nA for the SXFive-FE instrument and to 7 kV and 20 or 50 nA for the JXA-8530FPlus instrument.

On the SXFive-FE microprobe, three spectra of the Fe Lα-Lβ X-ray lines were recorded on each sample. The spectra were measured using Probe for EPMA in step-by-step acquisition mode (in opposition to the continuous ROM mode), from 0.685 to 0.733 keV with 511 steps and a dwell time of 1.8 s/step for the LTAP and TAP crystals and from 0.583 to 0.893 keV with 1.5 s/step for the PC0 pseudocrystal, resulting in an acquisition time of 13 minutes per scan. The spectra recorded with the PC0 crystals were wide enough to encompass the Fe Lℓ X-ray line. Other spectrometers did not record this line. The EDS spectrum was recorded from 0 to 20 keV using 2048 channels and a live time of 90 seconds. On the JEOL instrument, three SXES spectra were also recorded and aggregated together on each sample. The spectra were acquired from 0.236 to 2.830 keV with 4096 channels and a total counting time of 15 min.

For each spectrum, the background near the studied X-ray lines was fitted and removed using a linear function for the TAP crystals, the SXES and the EDS, and using an exponential curve for the PC0 crystal. The corrected spectra were then integrated by numerical analysis using the trapezoidal rule to calculate the total recorded Fe Lα+Lβ X-ray line intensity. To only calculate the Fe Lα or Fe Lβ X-ray intensity, as detailed below, the spectra were fitted with a set of pseudo-Voigt functions (weighted sum of a Gaussian and Lorentzian functions) using a non-linear fitting algorithm applying the Levenberg-Marquart (Levenberg 1944; Marquardt 1963) minimization

200 procedure and then integrated analytically. The Fe Lℓ X-ray spectrum was also fitted using pseudo-
201 Voigt functions to resolve the X-ray line from the Fe Lη X-ray line.

202 **How does carbon contamination affect spectral shapes?**

203 Acquisitions of detailed spectra require prolonged counting time. The carbon contamination that
204 builds up over time due to the electron beam interactions on the surface of the sample may affect
205 the measurements (Buse and Kearns 2015; Gopon et al. 2015) and distort the recorded spectrum.
206 Note that the use of a dry pumped system (without oil pumps) as well as a cold stage help reduce
207 the formation of carbon contamination. Any significant amount of carbon contamination created
208 during the acquisition may distort the spectra by decreasing the energy of the primary electrons
209 reaching the Fe-sulfide material and by increasing the absorption of the emitted X-rays as they
210 have to travel through the contamination layer before exiting the sample. These effects would be
211 more marked at the end of the acquisition when the carbon contamination has accumulated
212 significantly, and could produce different appearances between two spectra recorded in opposite
213 movement directions on a same spectrometer. The UW-Madison SXFive-FE instrument is
214 equipped with a custom cryo-chiller that cools the cold plate under the annular BSE detector to
215 reduce the amount of carbon contamination on the analysis spot. This anticontamination system
216 reduced the temperature of the cold plate in the microprobe chamber to values as low as about –
217 70°C and improved the chamber vacuum to a pressure as low as 5×10^{-6} Pa.

218 To investigate the effects of carbon contamination on the spectral acquisitions we performed
219 spectral scans at the same conditions as our analytical sessions with the SXFive-FE instrument by
220 recording the spectrum using a TAP, a LTAP and a PC0 monochromator crystal, scanning from
221 low to high X-ray energies and then from high to low X-ray energies on a fresh new spot. For each
222 direction, three spectra were acquired and averaged together to reduce the fluctuations due to the

counting statistics. The spectra were recorded under similar conditions as previously described: in step-by-step mode, with 511 steps and for X-ray energies ranging from 0.685 to 0.733 keV for the LTAP crystal, from 0.680 to 0.728 keV for the TAP crystal, and from 0.583 to 0.892 keV for the PC0 pseudocrystal. At the time of these measurements, the temperature of the cryo-chiller was of -33°C, potentially exacerbating the effects of the carbon contamination, if any, compared to the temperature at which the previous spectra (reported in the "spectra acquisition" section) were recorded. The measurements were performed on three samples covering a broad range of Fe concentrations: pure Fe, pyrite and stannite.

As seen on Figure 2, the recorded spectra show no significant variations on either peak shape or intensity for both the background and the tails of the Fe Lα and Fe Lβ X-ray lines. The only noticeable difference is a small reduction of the Fe Lα maximum X-ray intensity and a slight increase of the Fe Lβ X-ray intensity when the spectra were recorded from high to low energies compared to spectra recorded in the opposite direction. This observation, which cannot be explained by counting statistics only, is in accordance with an increase of the carbon contamination during the course of the measurement. However, the majority of the disparities between the spectra are typically within the uncertainties of the measurements due to the counting statistics. These uncertainties are represented for every 3 points by the error bars on Figure 2. The variations of the X-ray line areas due to carbon contamination and counting statistics remain generally small, as seen by the difference spectra shown on Figure 2, with average relative standard deviations (calculated from areas of spectra measured in opposite directions) of 0.7% for the LTAP crystal, of 3.6% for the TAP crystal and of 1.6% for the PC0 crystal. The worst case observed amongst all the recorded spectra was measured on the pure Fe standard by the low detection efficiency TAP crystal and had a relative standard deviation of about 4%. The fact that the deviation on the LTAP

spectrometer is very low indicates that carbon contamination has limited effect on the measurements at these experimental conditions when a cryo-chiller is used. It also indicates that the higher deviations seen on the spectra measured with the TAP and PC0 spectrometers, which were measured at the same time that the spectra measured on the LTAP spectrometers, are mostly due to the counting statistics.

On the JEOL JXA-8530FPlus microprobe, no anti-contamination devices were utilized but the measured area k-ratios are in good agreement, within the uncertainties due to counting statistics, with the area k-ratios measured on the CAMECA SXFive-FE microprobe using the cryo-chiller anticontamination device. This can easily be explained by assuming that the contamination rate is the same between samples for a given instrument. Hence, each spectrum is affected by the same X-ray intensity reduction due to the carbon contamination which is then canceled out when calculating the area k-ratios. The area k-ratios obtained between instruments are then similar. This shows that the effect of the carbon contamination does not significantly affect the measurements, even when no cryo-chiller devices are used. Nevertheless, to be consistent, all the measurements used to derive the calibration curves were obtained from spectra acquired in the direction of decreasing X-ray energy (except for the SXES and EDS detectors where the spectrum is acquired simultaneously).

Results

Quantification of Fe using the traditional method with the Fe Lα X-ray line

An attempt was made to quantify the Fe-sulfides at 7 kV and 90 nA with the traditional quantification method using the background-corrected Fe Lα X-ray peak intensities (measured at

the top of the X-ray peak and off to the sides to remove the background) with the PAP model (Pouchou and Pichoir 1991) and the MAC30 mass absorption coefficients (MACs) (Heinrich 1987) and using pure Fe or pyrite as a standard. The measurements were performed on the SXFive-FE instrument using a LTAP monochromator crystal and at least three points were measured on each sample. Figure 3 shows the measured iron content in the different samples as a function of the Fe content (previously measured at 15 kV with the traditional Fe Kα X-ray line). The results present significant deviations from the known Fe concentration. The error in the quantification, increases with the Fe content and can account up to 20 wt% (in absolute value) in the worst case when using pure Fe as a standard and up to 30 wt% when using pyrite as a standard. The error bars of the Fe concentration obtained using the Fe Lα line are on average of 2% for both standards, with a maximum of 5.6% and 5.0% for the Czamanske35 ZnFeS sample when using pure Fe and pyrite as a standard, respectively.

Quantification of Fe using the Fe Lℓ X-ray line and the traditional method

Gopon et al. (2013) showed that the Fe Lℓ X-ray line (L_3-M_1 transition) can successfully be used to quantify Fe in Fe-silicide samples. The spectra measured with the PC0 crystal were wide enough to record the Fe Lℓ and Fe Lη (L_2-M_1 transition) X-ray lines. The X-ray intensity, measured at the peak maximum, for the Fe Lℓ line was obtained by fitting the experimental spectrum (Figure 4). The background in this energy range and for this monochromator crystal is best fitted by an exponential function rather than a linear function. The proximity of the more intense Fe Lα-Lβ lines prevents the acquisition of the background on the high energy side of the Fe Lη line. This requires the acquisition of the X-rays far from the Fe Lℓ line on the high energy side of the Fe Lα-Lβ spectrum to be able to correctly evaluate the background. The Fe Lℓ and Lη lines were deconvoluted using pseudo-Voigt functions. As seen on Figure 4, the Lη line does not interfere

strongly with the Lℓ line: its intensity, at the X-ray energy of the maximum of the Fe Lℓ line, is about ~1% to 1.5% of the maximum X-ray intensity of the Fe Lℓ line. This value, however, could change with other monochromator crystals having different spectral resolutions (e.g., TAP vs PC0 crystals). It should be noted that this interference is not a problem as long as the Lℓ and Lη X-ray intensity ratio remains constant between unknowns and standards, and can be seen as the classical Kα1, Kα2 interference. The net X-ray intensities corresponding to the maximum of the Fe Lℓ lines were extracted from the fits and used to calculate k-ratios relative to pure Fe. These k-ratios were processed using Probe for EPMA (Donovan et al. 2021) and BadgerFilm (Moy and Fournelle 2021) by specifying the other element abundances (previously measured at 15 kV). The PAP $\phi(\rho z)$ model (Pouchou and Pichoir 1991) was used in the matrix correction procedure, as well as the FFAST MACs (Chantler et al. 2005) for Probe for EPMA and the MAC30 MACs for BadgerFilm (the MAC30 MACs cannot be used for the Lℓ line in Probe for EPMA). The obtained Fe concentrations are displayed in Table 3.

Generally good quantification numbers were obtained at 7 kV using the Fe Lℓ X-ray line compared to the results obtained at 15 kV using the Fe Kα line. The greatest deviation was obtained for the cobaltite sample with a relative deviation of -5.72%. One disadvantage of using the Fe Lℓ X-ray line for quantification is that compared to the Lα X-ray line, the X-ray intensity of the Lℓ line is weak, which can be problematic especially for low Fe concentration specimens. This leads to greater statistical fluctuations in the measured spectrum, to a less accurate fitting and hence to a less accurate measured net X-ray intensity making its use difficult to quantify low Fe concentration samples. Higher beam currents or longer counting times can be used to overcome this problem, with the downside of potentially damaging the sample and increasing carbon contamination effects. It should also be noted that the Fe Lℓ line is interfered by the second order of diffraction of the Mg

Kα X-ray line, making its use for quantification difficult in Mg-bearing samples (not the case here). For these reasons, the authors evaluated alternative Fe Lα-Lβ approaches for low kV EPMA of silicates (Moy et al. 2019b).

Fe Lα+Lβ area k-ratio vs. Fe content

As shown above (Figure 3) and in previous works (Gopon et al. 2013; Llovet et al. 2016; Buse and Kearns 2018; Moy et al. 2019a, 2019b), the traditional quantification method is not suitable for quantification using the Fe Lα X-ray line. This is due to a multitude of reasons, such as large uncertainties in the knowledge of the MACs close to the absorption edges, which is the case for the soft X-ray lines such as Fe Lα. These MACs can vary strongly from one material to another due to chemical bonding effects. Attempts have been made to measure the Lα MACs, as well as other atomic parameters such as the fluorescence yield, of Ni in Ni-Si samples (Heikinheimo et al. 2016; Llovet et al. 2016) and of Fe in olivines (Buse and Kearns 2018). These works showed, to some extent, an improvement of the experimental results. However, in addition to these problems, we have shown that the theory behind the matrix correction procedure is not valid close to the absorption edges, e.g., the Fe Lα X-ray line, and it is not possible to accurately measure the MACs close to absorption edges using traditional WDSs (see Moy et al., 2019b for a full explanation).

Lα+Lβ area k-ratio calibration curve

The recent studies by Moy et al. (2019 a, b) describe an alternative approach for quantifying Fe contents at low kV that overcomes the accuracy problem using the traditional Fe Lα EPMA approach and when Fe Lℓ is not applicable. We evaluate below its applicability to Fe-sulfides. In this approach, an empirical curve is defined which uses "area k-ratios", integrating the background-

This is the peer-reviewed, final accepted version for American Mineralogist, published by the Mineralogical Society of America.
The published version is subject to change. Cite as Authors (Year) Title. American Mineralogist, in press.
DOI: https://doi.org/10.2138/am-2022-8027. http://www.minsocam.org/

subtracted areas under the Fe Lα+Lβ peaks and ratioing them to the same integrated area of an Fe-rich standard, here Fe metal. This approach actually is a re-tooled version of one of Castaing's original methods for quantification in his original electron probe dissertation (Castaing 1951), which became known as the alpha-factor correction method (Ziebold and Ogilvie 1963) and then the Bence-Albee correction method (Bence and Albee 1968).

The area k-ratios of the combined Fe Lα-Lβ X-ray lines, measured at 7 kV and a takeoff angle of 40°, were obtained on each Fe sulfide sample relative to the same X-ray lines' area obtained on a pure Fe standard. Figure 5 shows the measured area k-ratios as a function of the known Fe concentration. The first significant observation is that the area k-ratio values are very close to each other for a given sample, irrespective of the spectrometer type (WDS, EDS or SXES) or instrument model used – and in accordance with the theoretical derivations given in the following section. The experimental area k-ratios follow a smooth increase with increasing Fe concentration up to about 40 wt%. However, at higher Fe concentrations, i.e., for the pyrite, pyrrhotite and troilite materials, the area k-ratio increases abruptly, deviating from the expected correlation. Indeed, pyrite which has an Fe concentration of about 47 wt%, has an area k-ratio similar to the area k-ratio measured on pyrrhotite and troilite, which have an Fe concentration of about 60-63 wt%. These materials, which have a similar matrix composition, should see an increase of the Fe Lα X-ray intensity with increasing iron content. However, as shown in Figure 6, the opposite behavior occurs: pyrite has a much stronger Fe Lα X-ray line intensity than pyrrhotite and troilite despite its lower Fe concentration. This behavior is not seen for the Fe Lβ X-ray intensity resulting in a similar Fe Lα+Lβ area k-ratios for these materials.

To circumvent this problem for modeling of those high-Fe sulfides, instead of calculating the Fe Lα+Lβ area k-ratio, the Fe Lα and Fe Lβ area k-ratios are calculated independently and then

averaged together. To calculate the two areas separately, because of their overlap, each spectrum is fitted with a set of Pseudo-Voigt functions which are then integrated analytically. The background was previously removed by fitting the tails of the spectrum with a linear or exponential function depending on the monochromator crystal used. Using this method, the area k-ratios of the pyrite, pyrrhotite and troilite can be distinguished from each other. Hence, two procedures have been developed here: the combined Fe Lα+Lβ area k-ratios can be used to obtain a calibration curve and to quantify Fe-sulfides with an Fe concentration lower than about 45 wt%, and the averaged k_{av}=(Fe Lα area k-ratio + Fe Lβ area k-ratio)/2 quantities can be used for higher Fe concentrations. Note that this technique is harder to use with data acquired with an EDS or with a WDS equipped with a PC0 or PC1 (2d = 60.79 Å) monochromator crystal because the low spectral resolution of these detectors does not allow the distinction between the Lα and the Lβ X-ray lines. This can be partially mitigated by fitting the low-resolution spectra using strong constraints such as the position of the Lβ line relative to the position of the Lα line. However, accuracy of such fits is difficult to assess and may lead to inaccuracies in the derivation of a calibration curve for high Fe concentration specimens.

Because the experimental k-ratios are almost identical from one spectrometer to another, in agreement with the theoretical derivations in the next section, data across instruments and spectrometers were averaged subsequently. The two sets of data (Fe concentrations below and above 45 wt%) follow a smooth increasing trend, as shown in Figure 7. However, the dataset of low Fe concentration samples has some “irregularities”: the stannite, cobaltite and arsenopyrite data are slightly off the curve defined by the other elements. The data were fitted by part, with polynomial functions with the conditions that the k-ratios are 0 and 1 for Fe concentrations of 0

This is the peer-reviewed, final accepted version for American Mineralogist, published by the Mineralogical Society of America.
The published version is subject to change. Cite as Authors (Year) Title. American Mineralogist, in press.
DOI: https://doi.org/10.2138/am-2022-8027. http://www.minsocam.org/

and 100 wt%, respectively. The low Fe concentration data were fitted with and without the stannite, cobaltite and arsenopyrite samples. The obtained polynomial equations (displayed in Figure 7) are:

Low Fe concentrations, without stannite cobaltite and arsenopyrite

$$C = -797.44 \times k^4 + 599.35 \times k^3 - 61.966 \times k^2 + 72.372 \times k \quad for\ C \leq 45\ wt\% \quad (1)$$

Low Fe concentrations, with stannite cobaltite and arsenopyrite

$$C = 32719.17 \times k^5 - 36588.61 \times k^4 + 13959.12 \times k^3 - 2063.446 \times k^2 + 176.4047 \times k \quad for\ C \leq 45\ wt\% \quad (2)$$

High Fe concentrations

$$C = 75.865 \times k_{av}^4 - 107.29 \times k_{av}^3 + 36.104 \times k_{av}^2 + 95.323 \times k_{av} \quad for\ C > 45\ wt\% \quad (3)$$

where C is the Fe concentration in wt%, k is the Fe Lα+Lβ area k-ratio (where pure Fe is the standard), and k_{av} is the (Fe Lα area k-ratio + Fe Lβ area k-ratio)/2 quantity. Very good regression factors of 0.996 and 0.999 were found for the fitting polynomials. The best fit of the low Fe concentration dataset was obtained for Fe-sulfides with Cu and/or Ni whereas the addition of samples containing other elements in the sulfide structure yielded more complicated and slightly poorer fit. This can be attributed to changes in X-ray production and emission caused by bonding effects due to the presence of non-divalent ions like Sn and As. Consequently, the area k-ratios from these Fe-sulfide samples differ from those only containing divalent cations like Fe, Cu and Ni. Therefore, we recommend using the simpler calibration curve that excludes the stannite, cobaltite and arsenopyrite data points (Eq. 1) when analyzing sulfides with only 4th-period transition metals as cations. For sulfide compositions outside of this compositional range such as arsenopyrite the calibration curve that includes all data points (Eq. 2) should be favored. It should also be noted that for the low Fe concentration calibration curve, there is no experimental data for the relevant Fe concentrations above 34.32 wt%. Consequently, the fitting is unconstrained above this value. This may result in some inaccuracies in the quantification predictions, in particular close to the limit of 45 wt%.

Discussion

This is the peer-reviewed, final accepted version for American Mineralogist, published by the Mineralogical Society of America.
The published version is subject to change. Cite as Authors (Year) Title. American Mineralogist, in press.
DOI: https://doi.org/10.2138/am-2022-8027. http://www.minsocam.org/

Theoretical derivation of the calibration curves

The statement above that these calibration curves are valid for all electron probe WDS, SXES or EDS detectors, provided they are acquired at 7 kV and with a takeoff angle of 40°, can be supported by a rigorous examination of the physics of X-ray generation, of spectral characteristics, and of detector behavior.

The X-ray intensity of a given X-ray line, emitted from the sample before detection by the spectrometer, can be written as follows:

$$I_X(E) = C_A \frac{N_a}{A_r}\, n_{el}\, \sigma_X^A(E_0)\, \mathcal{L}(E) \int_0^\infty \varphi_i(\rho z) e^{-\frac{\mu}{\rho}(E)\frac{\rho z}{\sin\theta_d}}\, d\rho z\ \mathcal{F} \qquad (4)$$

where $I_x(E)$ is the number of characteristic X-rays originating from the inner shell transition of interest and emitted at the photon energy E per unit of time. C_A and A_r represent the concentration and the atomic mass of the element A of interest, respectively. N_a denotes the Avogadro number. It is worth noting that the product $C_A \frac{N_a}{A_r}$ by the material density ρ gives the number of atoms A per unit volume. n_{el} is the number of primary electrons reaching the sample per unit of time. This quantity can be calculated by j/q where j is the current of the primary electron beam, in amperes, and q is the electric charge of an electron, i.e., ~1.602×10^{-19} coulomb. $\sigma_X^A(E_0)$ is the X-ray production cross section, in cm², of the considered X-ray line by impact of an electron with an energy E_0. $\sigma_X^A(E_0)$ takes into account the ionization cross section by electron impact of the shell (or subshell) i generating the considered X-ray line and also the ionization cross section of all the inner-shells that can produce an electron vacancy in the shell i during the atomic relaxation process – this includes radiative, non-radiative, Coster-Kronig and super-Coster-Kronig transitions (Moy

This is the peer-reviewed, final accepted version for American Mineralogist, published by the Mineralogical Society of America.
The published version is subject to change. Cite as Authors (Year) Title. American Mineralogist, in press.
DOI: https://doi.org/10.2138/am-2022-8027. http://www.minsocam.org/

et al. 2013). For example, the X-ray production cross section of the $L\alpha_1$ X-ray line by transition of an electron from the M_5 subshell to the L_3 subshell can be written:

$$\sigma^A_{L_{\alpha 1}}(E_0) = \omega^A_{L_3} \frac{\Gamma^A_{L_3-M_5}}{\Gamma^A_{L_3-total}} \left[Q^A_{L_3}(E_0) + Q^A_{L_2}(E_0) \times f_{23} + Q^A_{L_1}(E_0) \times (f_{13} + f_{12}f_{23} + f'_{13}) + Q^A_K(E_0) \times (\eta_{K-L1}(f_{13} + f_{12}f_{23} + f'_{13}) + \eta_{K-L2}f_{23} + \eta_{K-L3})\right] \quad (5)$$

where $\omega^A_{L_3}$ is the fluorescence yield of the element A for an electron vacancy in the subshell L_3 (i.e., the probability to emit a photon during the relaxation of atom A with an initial vacancy in the electronic subshell L_3). $\Gamma^A_{L_3-M_5}$ is the partial radiative width associated to the L_3–M_5 transition and $\Gamma^A_{L_3-total}$ is the total radiative width for all possible transitions to the L_3 subshell. This ratio corresponds to the probability that amongst all the possible electron transitions, the relaxation occurs by the transition of an electron from the subshell M_5 to the vacancy located in the subshell L_3. $Q^A_i(E_0)$ is the ionization cross section of the shell or subshell i by impact of electrons of energy E_0. f_{ij} is the Coster-Kronig yield (i.e., the probability that a vacancy in the subshell L_i of a singly ionized atom shifts to a higher subshell L_j of the same shell) and f'_{13} is the radiative transition yield between the L_1 and L_3 subshells. The terms $\eta_{K\text{-}Li}$ are the radiative plus non-radiative yields for the transitions of vacancies from the K shell to the L_i subshell. In Eq. (4), $\mathcal{L}(E)$ represents the natural shape of the X-ray line, whose area is normalized to unity. Due to the uncertainty principle of quantum mechanics, the characteristic X-rays are emitted with a distribution following a Lorentzian function of the form:

$$\mathcal{L}(E) = \frac{H_L}{1 + 4\left(\frac{E - E_X}{\Gamma}\right)^2} \quad (6)$$

where H_L is the maximum of the function, Γ is the full width at half maximum and E_X is the energy on which the function is centered. The $\varphi_i(\rho z)$ term is the so-called phi-rho-z function corresponding

the ionization depth distribution of the electron shell (or subshell) i of element A at mass depth ρz inside the sample for an incident electron beam of energy E_0.

The next term in Eq. (4), represented by the exponential factor, accounts for the attenuation of the X-rays generated inside the sample before they reach the surface with an angle θ_d (corresponding to the takeoff angle of the spectrometer). $\frac{\mu}{\rho}(E)$ is the mass absorption coefficient, in cm²/g, of the material composing the sample for a photon of energy E. It is worth noting that the term $\frac{\mu}{\rho}(E)$ varies rapidly as a function of the photon energy close to the ionization edges. Finally, $\mathscr{F}$ represents the enhancement of X-rays by secondary fluorescence from other characteristic X-rays and from the bremsstrahlung ($\mathscr{F} \geq 1$).

The emitted X-ray intensity $I_X(E)$ is then recorded by the spectrometers at the X-ray energy E_i (not necessarily the line center E_X):

$$I(E_i) = \int_{-\infty}^{+\infty} I_X(E) \frac{\Delta\Omega}{4\pi} \varepsilon(E) \mathcal{G}(E_i - E)\, dE \approx \int_{E_i-\Delta E/2}^{E_i+\Delta E/2} I_X(E) \frac{\Delta\Omega}{4\pi} \varepsilon(E) \mathcal{G}(E_i - E)\, dE \qquad (7)$$

where ε(E) and $\frac{\Delta\Omega}{4\pi}$ are the intrinsic detection efficiency and the geometric detection efficiency of the spectrometer for photons of energy E, respectively. Because of the "imperfect" spectrometer response function, X-rays with energies in a small interval (or energy bin width) centered around the recorded X-ray energy E_i and with a width ΔE will also be detected. The spectrometer response function can be better described by a gaussian function, here denoted $\mathcal{G}(E_i - E)$ with a full width at half maximum of Γ_G (here $3\Gamma_G \approx \Delta E$), a height H_G and centered at the photon energy E_i.

In the traditional case where ε(E) and $\frac{\mu}{\rho}(E)$ are almost constant in the energy interval ΔE (which is almost always the case for ε(E), except, for example, close to an absorption edge caused by the

This is the peer-reviewed, final accepted version for American Mineralogist, published by the Mineralogical Society of America.
The published version is subject to change. Cite as Authors (Year) Title. American Mineralogist, in press.
DOI: https://doi.org/10.2138/am-2022-8027. http://www.minsocam.org/

spectrometer separation window or by an absorption edge of the gas used in proportional counters), the detected X-ray intensity becomes:

$$\mathrm{I}(E_i) = C_A \frac{N_a}{A_r}\, n_{el}\, \sigma_X^A(E_0) \int_0^{\infty} \varphi_i(\rho z) e^{-\frac{\mu}{\rho}\frac{\rho z}{\sin\theta_d}}\, d\rho z\ \mathcal{F}\ \frac{\Delta\Omega}{4\pi}\varepsilon \int_{-\infty}^{+\infty} \mathcal{G}(\mathrm{E}_i - E)\mathcal{L}(\mathrm{E})\, dE \qquad (8)$$

Hence, in the traditional case, after cancelling out identical factors between the numerator and denominator, the k-ratio is given by:

$$k = \frac{\mathrm{I}_u(E_i)}{\mathrm{I}_s(E_i)} = \frac{C_A^u \int_0^{\infty} \varphi_i^u(\rho z) e^{-\frac{\mu}{\rho}\Big|_u \frac{\rho z}{\sin\theta_d}}\, d\rho z\ \mathcal{F}_u}{C_A^s \int_0^{\infty} \varphi_i^s(\rho z) e^{-\frac{\mu}{\rho}\Big|_s \frac{\rho z}{\sin\theta_d}}\, d\rho z\ \mathcal{F}_s} \qquad (9)$$

where the indices u and s stand for unknown and standard, respectively. It was assumed that the same beam current was used, i.e., the same number of electrons (per unit of time) reached the unknown and the standard. As seen in Eq. (9), this k-ratio is independent of the spectrometer characteristics. However, when the MACs vary in the energy bin width ΔE, the emitted X-ray intensity $\mathrm{I_X(E)}$ cannot be extracted from the integral in Eq. (7) and thus, the k-ratio expression cannot be simplified (the spectrometer contributions remain). This is the case close to the ionization edge where the MACs strongly vary with respect to the X-ray energy. Also, the k-ratio expression cannot be simplified when the natural line shape $\mathcal{L}(\mathrm{E})$ of the X-ray line is different between the unknown and the standard, which could be the case for the soft X-rays where bonding effects can change the density of state of the outer electron shells and hence the shape of the associated characteristic X-ray line, or when the X-ray production cross section differs from the standard and the unknown, which can also be caused by bonding effects. In these situations (present near absorption edges), the k-ratio remains:

This is the peer-reviewed, final accepted version for American Mineralogist, published by the Mineralogical Society of America.
The published version is subject to change. Cite as Authors (Year) Title. American Mineralogist, in press.
DOI: https://doi.org/10.2138/am-2022-8027. http://www.minsocam.org/

480

$$k = \frac{\mathrm{I}_u(E_i)}{\mathrm{I}_s(E_i)} = \frac{C_A^u\ \sigma_X^{A,u}(E_0)\ \int_{-\infty}^{+\infty}\int_0^{\infty}\varphi_i^u(\rho z)e^{-\frac{\mu}{\rho}(E)\Big|_u\frac{\rho z}{\sin\theta_d}}\,d\rho z\,\mathcal{G}(\mathrm{E}_i-E)\mathcal{L}(\mathrm{E})dE\ \mathcal{F}_u}{C_A^s\ \sigma_X^{A,s}(E_0)\ \int_{-\infty}^{+\infty}\int_0^{\infty}\varphi_i^s(\rho z)e^{-\frac{\mu}{\rho}(E)\Big|_s\frac{\rho z}{\sin\theta_d}}\,d\rho z\,\mathcal{G}(\mathrm{E}_i-E)\mathcal{L}(\mathrm{E})\mathrm{dE}\ \mathcal{F}_s} \tag{10}$$

481

482 and cannot be further simplified. These k-ratios depend on the spectrometer response function $\mathcal{G}$
483 and then may be different from on spectrometer to another. The determination of C_A^u is also almost
484 impossible as most of the parameters used in Eq. (10) (especially $\frac{\mu}{\rho}(E)$, $\mathcal{G}(\mathrm{E}_i - E)$ and $\mathcal{L}(\mathrm{E})$) are
485 not well known, particularly for the soft X-rays. Fortunately, by calculating the area k-ratio, i.e.,
486 the area of the X-ray lines calculated over the X-ray energy for both the unknown and the standard,
487 and by using the property of the convolution product that states that the area under a convolution
488 of factors is the product of areas under these factors, the area k-ratio can be written as:

$$\begin{aligned} k_{Area} &= \frac{\int_{-\infty}^{+\infty}\mathrm{I}_u(E_i)dE_i}{\int_{-\infty}^{+\infty}\mathrm{I}_s(E_i)dE_i} \\ &= \frac{C_A^u\sigma_X^{A,u}(E_0)\mathcal{F}_u\int_{-\infty}^{+\infty}\int_0^{\infty}\varphi_i^u(\rho z)e^{-\frac{\mu}{\rho}(E)\Big|_u\frac{\rho z}{\sin\theta_d}}\,d\rho z\,\mathcal{L}(\mathrm{E})dE\ \int_{-\infty}^{+\infty}\mathcal{G}(\mathrm{E}_i-E)dE}{C_A^s\sigma_X^{A,s}(E_0)\mathcal{F}_s\int_{-\infty}^{+\infty}\int_0^{\infty}\varphi_i^s(\rho z)e^{-\frac{\mu}{\rho}(E)\Big|_s\frac{\rho z}{\sin\theta_d}}\,d\rho z\,\mathcal{L}(\mathrm{E})\mathrm{dE}\ \int_{-\infty}^{+\infty}\mathcal{G}(\mathrm{E}_i-E)dE} \end{aligned} \tag{11}$$

489

490 The spectrometer broadenings $\int_{-\infty}^{+\infty}\mathcal{G}(\mathrm{E}_i - E)dE$ cancel out in the numerator and denominator and
491 the remaining quantities are independent of the spectrometer used. Although the area k-ratio cannot
492 be calculated analytically because of our lack of knowledge of the different parameters, a
493 calibration curve can be obtained by measuring the area k-ratios on samples of known
494 compositions. This calibration curve is independent of the spectrometer used and can thus be
495 employed on any instrument with any spectrometer, as long as the electron beam energy E_0 and the
496 spectrometer takeoff angle θ_d used to acquire the calibration curve are the same as used here.

497 The derivation of a calibration curve using the traditional k-ratio obtained by measuring the X-ray
498 intensity at the maximum of the peak and on each side to remove the background, on the unknown
499 and on a standard, is also possible, but that curve will not be spectrometer independent and must
500 be redetermined on each instrument and each spectrometer, as shown in Eq. (10). The derivation
501 was done for one characteristic X-ray line. In the case of several overlapping X-ray lines, as it is
502 generally the case for the Fe Lα and Lβ X-ray lines using PC0 diffracting crystals, the area k-ratio
503 can be obtained similarly by integrating over the extent of the overlapping lines. This theoretical
504 derivation explains why the area k-ratio values displayed on Figure 5 are similar between the
505 different instruments and the different spectrometers.

506

507 **Using the calibration curve on a different instrument**

508 For an initial test of the validity of our calibration curves, the same calibration samples were
509 examined using a different microprobe instrument, a W-filament CAMECA SX51 microprobe
510 located at the Eugene Cameron electron microscopy laboratory, Department of Geoscience,
511 University of Wisconsin-Madison. The Fe Lα and Lβ spectra were recorded at 7 kV and 50 nA
512 using two TAP crystals (2d = 25.745 Å) and a PC0 (2d = 45.0 Å) crystal. Three spectra were
513 recorded for each sample and aggregated together to reduce the counting fluctuations and to smooth
514 the spectra. The spectra were recorded, with 300 steps and a dwell-time of 2 s/step, from 688 to
515 733 eV for the TAP crystals and from 588 to 878 eV for the PC0 crystal. The takeoff angle of the
516 spectrometers used was 40°. To remove the background, the spectra were fitted with a linear
517 function for the TAP crystals and with an exponential function for the PC0 crystal. The Fe Lα and
518 Lβ X-ray lines were fitted with pseudo-Voigt functions to calculate area k-ratios relative to pure

519 Fe. The calibration curves deduced from the previous results (Eqs. 1–3) and shown in Figure 7
520 were used to quantify Fe in the samples. As shown on Figure 8, and Table 4, generally good
521 quantification results were obtained, especially when compared to the traditional matrix correction
522 quantification method (Figure 3). The quantification of the sample Czamanske37, with nominal Fe
523 concentration of 23.16 wt%, is systematically underestimated by the calibration curve method with
524 an obtained average Fe concentration of 20.08 wt%. Despite this outlier sample, the maximum
525 quantification error was of 3.2 wt% obtained on the pyrrhotite specimen with a TAP crystal. The
526 quantification error, in average, was of 1.3 wt% for the TAP crystals and of 0.9 wt% for the PC0
527 crystal. The observed errors (deviation from the diagonal) are consistent with counting statistics.

528 The results are in generally good agreement with the expected Fe concentrations, demonstrating
529 the robustness of the calibration curve approach, irrespective of instrument, spectrometer, and
530 crystal choices. It should also be noted that the area calibration curve is not affected by spectrometer
531 drifts as the entire spectrum is recorded and integrated.

532 To show the improvements obtained on the quantification of Fe by using the calibration curve with
533 regard to the traditional quantification method using the Fe Lα X-ray line, a direct comparison of
534 the results obtained with the two methods is displayed in Table 5. The quantification results
535 obtained with the calibration curve on the SX51 instrument, using the spectrometer #1 (TAP
536 crystal) were compared to the results obtained on the SXFive-FE instrument with the spectrometer
537 #1 (LTAP crystal) using the Fe Lα line and the traditional method. Both methods were using pure
538 Fe as standard. The results were also compared to the quantification results obtained at 15 kV using
539 the Fe Kα X-ray lines.

Better quantification results were obtained with the calibration curve method except for the stannite specimen where the Fe concentration is underestimated (2.18 wt% below the nominal value). Systematic substantial improvements were obtained for the high Fe concentration samples.

Using the calibration curve to quantify unknown Fe-sulfide specimens

Unknown Fe-sulfide samples were used to test the predictions of the area k-ratio calibration curves as well as quantification results obtained using the Fe Lℓ X-ray lines. The three samples used were pyrrhotite from Galax, VA, chalcopyrite from Durango, Mexico and bornite from the Magma mine, AZ. These samples were first analyzed at 15 kV and 20 nA using the traditional Kα lines on the SXFive-FE instrument to determine their exact compositions. PET crystals were used to measure the S Kα lines and LLiF crystals were used to measure the Fe Kα and Cu Kα X-ray lines. The quantification results are displayed in Table 6.

Spectra of the Fe Lα and Lβ X-ray lines as well as the spectrum of the Fe Lℓ X-ray line were recorded at 7 kV and 70 nA using a LTAP and a PC0 crystals on the SXFive-FE instrument. PHAs were set to wide differential mode. Three spectra were recorded and averaged together for each sample. The averaged spectra were corrected from the continuum and fitted with pseudo-Voigt functions to calculate the area k-ratios, relative to pure Fe. The obtained Fe Lα+Lβ area k-ratios for the chalcopyrite and bornite specimens and the (Fe Lα k-ratio + Fe Lβ k-ratio)/2 quantity for the pyrite specimen were used with the calibration curves to determine the Fe content for each sample. The Fe Lℓ X-ray intensities were processed with CalcZAF using the FFAST MAC database, as well as with BadgerFilm using the MAC30 MACs. Both programs were using the PAP matrix correction algorithm. Quantification results are displayed in Table 7.

Using the calibration curves or the Fe Lℓ X-ray line intensity leads to significant quantification improvements compared to the traditional quantification method using the Fe Lα X-ray line. For the low Fe concentration sample, the calibration curve method underestimates the concentration by 4 wt% in average while the Fe Lℓ method gives very good results with an overestimation of only 0.22 wt% in average.

Implications

Sulfides are the source for most of the world supplies of non-ferrous metals and their synthetic analogues are of interest to physicists and material scientists for their electrical, magnetic, and optical properties. However, grain sizes can be in the sub-micrometer range or occur as narrow overgrowths or exsolutions below the spatial limit of traditional EPMA analysis at 15 kV or higher. Quantifying iron contents in sulfides at low accelerating voltage successfully is a necessary procedure for measuring these sub-micrometer sulfide grains by EPMA. We have shown that when accelerating voltages much lower than 15-20 kV must be used, two new approaches can avoid the problems encountered when utilizing Fe Lα X-ray peak intensities combined with traditional matrix correction methods and provide generally good results at that reduced voltage. The first one utilizes the low intensity Fe Lℓ X-ray line but may be limited in its use to samples (1) with Fe-concentration larger than trace level because of the low Fe Lℓ X-ray line intensity, and (2) to Mg-poor phases like sulfides because of an interference by the second order of diffraction of the Mg Kα line. The second approach uses a calibration curve method and exploits the more intense Fe Lα-Lβ X-ray peak area intensities to calculate area k-ratios relative to a standard. This approach yields generally good Fe quantification results even at low Fe abundances. The best quantification

583 results were obtained for Fe-sulfides with Cu and/or Ni whereas the presence of other elements in
584 the sulfide structure made the quantification more difficult. This probably reflects changes in
585 production and emission of X-rays due to changes in bonding environment in the presence of ions
586 like Sn and As. This can result in area k-ratios differing from sulfides only containing divalent
587 cations like Fe, Cu and Ni, and would explain why these specimens are more difficult to fit with a
588 general calibration curve. Another advantage of the calibration curve method is that labs can readily
589 apply the curve determined in this study to data acquired on their instrument and spectrometers as
590 long as they also utilize an accelerating voltage of 7 kV and the spectrometer has a takeoff angle
591 of 40°. Our universal calibration curve utilizes pure Fe metal, a widely available standard material,
592 and thereby offers an easy and fast method to quantify Fe in sulfides using the Fe Lα-Lβ and/or Fe
593 Lℓ X-ray lines at low kV. Alternatively, a new calibration curve can be determined, provided that
594 a similar suite of reference materials is available, for either a different accelerating voltage and/or
595 an instrument with a different takeoff angle (e.g., SEM-WDS). In addition, the method is well
596 suited to high-spectral resolution, parallel channel X-ray detectors such as the SXES (JEOL Inc.),
597 and to a lesser extent EDS, as these detector types acquire the entire Fe L X-ray spectrum
598 simultaneously. The time-advantage presented by this method may be further compounded if other
599 transition metals like Cr, Ni, Cu, Zn are present, and it can be established that they also can be
600 quantified by calibration curves (von der Handt, Moy and Fournelle, in progress). Although the
601 presence of the SXES detectors in microanalysis labs is currently still scarce, they could certainly
602 play an essential role in the future, especially in the geosciences.

603 The successful application of the calibration curve method to low kV quantitative analysis of iron
604 in sulfides extends our findings on Fe-silicides (Moy et al. 2019a) and olivines (Moy et al. 2019b)

605 and provides a roadmap to future investigation of more complex iron-bearing phases and a wider
606 range of accelerating voltages.

607 **Acknowledgments**

608 We would like to thank the two reviewers of the manuscript, Michael Jercinovic and an anonymous
609 reviewer, as well as Associate Editor Antonio Acosta-Vigil for their useful comments in the
610 improvement of the manuscript. Support for this research came from the National Science
611 Foundation: EAR-1337156 (JHF), EAR-1554269 (JHF), EAR-1849386 (JHF) and EAR-1849465
612 (AVDH).

613 **References**

614 Bence, A.E., and Albee, A.L. (1968) Empirical Correction Factors for the Electron Microanalysis
615 of Silicates and Oxides. The Journal of Geology, 76, 382–403.

616 Buse, B., and Kearns, S. (2015) Importance of Carbon Contamination in High-Resolution (FEG)
617 EPMA of Silicate Minerals. Microscopy and Microanalysis, 21, 594–605.

618 ——— (2018) Quantification of Olivine Using Fe Lα in Electron Probe Microanalysis (EPMA).
619 Microscopy and Microanalysis, 24, 1–7.

620 Castaing, R. (1951) Application of Electron Probes To local chemical and crystallographic
621 analysis. Ph. D. Thesis, University of Paris.

622 Chantler, C.T., Olsen, K., Dragoset, R.A., Chang, J., Kishore, A.R., Kotochigova, S.A., and
623 Zucker, D.S. (2005) X-Ray Form Factor, Attenuation and Scattering Tables (version 2.1).
624 National Institute of Standards and Technology.

625 Czamanske, G.K., and Ingamells, C.O. (1970) Selective chemical dissolution of sulfide minerals:

626 a method of mineral separation. American Mineralogist, 55, 2131–2134.

627 Deines, P., and Harris, J.W. (1995) Sulfide inclusion chemistry and carbon isotopes of African
628 diamonds. Geochimica et Cosmochimica Acta, 59, 3173–3188.

629 Desborough, G.A., Heidel, R.H., and Czamanske, G.K. (1971) Improved Quantitative Electron
630 Micro-Probe Analysis at Low Operating Voltage : II. Sulfur. American Mineralogist, 56,
631 2136–2141.

632 Donovan, J.J., Kremser, D., Fournelle, J., and Goemann, K. (2021) Probe for EPMA v. 12.9.5
633 User's Guide and Reference, 430 p. Probe Software, Inc.

634 Fournelle, J. (2006) Silicate Peak Shifts , Spectrometer Peaking Issues and Standard / Specimen
635 Size Discrepancies in EPMA : 3 Bumps in the Road to the Goal of 1 % Accuracy. In AGU
636 Transactions.

637 Gopon, P., Fournelle, J., Sobol, P.E., and Llovet, X. (2013) Low-Voltage Electron-Probe
638 Microanalysis of Fe–Si Compounds Using Soft X-Rays. Microscopy and Microanalysis, 19,
639 1698–1708.

640 Gopon, P., Sobol, P., and Fournelle, J. (2015) Non-Sequential Spectral Acquisitions and Data
641 Reconstruction to Remove Time-Dependent Effects from X-Ray Spectra. Applied
642 Spectroscopy, 69, 1403–1411.

643 Harries, D., and Langenhorst, F. (2013) The nanoscale mineralogy of Fe,Ni sulfides in pristine
644 and metamorphosed CM and CM/CI-like chondrites: Tapping a petrogenetic record.
645 Meteoritics and Planetary Science, 48, 879–903.

646 Heikinheimo, E., Pinard, P.T., Richter, S., Llovet, X., and Louhenkilpi, S. (2016) Electron probe

microanalysis of Ni-silicides at low voltage: Difficulties and possibilities. IOP Conference Series: Materials Science and Engineering, 109.

Heinrich, K.F.J. (1987) Mass absorption coefficients for electron probe microanalysis. (J.D. Brown & R.H. Packwood, Eds.)Proc. ICXOM XI, 67–119.

Jercinovic, M.J., Williams, M.L., Allaz, J., and Donovan, J.J. (2012) Trace analysis in EPMA. IOP Conference Series: Materials Science and Engineering, 32, 012012.

Kearns, S., Buse, B., and Wade, J. (2014) Mitigating Thermal Beam Damage with Metallic Coats in Low Voltage FEG-EPMA of Geological Materials. Microscopy and Microanalysis, 20, 740–741.

Kubo, Y., Hamada, K., and Urano, A. (2013) Minimum detection limit and spatial resolution of thin-sample field-emission electron probe microanalysis. Ultramicroscopy, 135, 64–70.

Levenberg, K. (1944) A method for the solution of certain non-linear problems in least squares. Quarterly of Applied Mathematics, 2, 164–168.

Llovet, X., and Salvat, F. (2017) PENEPMA: A Monte Carlo Program for the Simulation of X-Ray Emission in Electron Probe Microanalysis. Microscopy and Microanalysis, 23, 634–646.

Llovet, X., Pinard, P.T., Heikinheimo, E., Louhenkilpi, S., and Richter, S. (2016) Electron probe microanalysis of Ni Silicides Using Ni-L X-Ray lines. Microscopy and Microanalysis, 22, 1233–1243.

Llovet, X., Moy, A., Pinard, P.T., and Fournelle, J.H. (2020) Electron probe microanalysis: a review of recent developments and applications in materials science and engineering.

668 Progress in Materials Science.

669 Marquardt, D. (1963) An Algorithm for Least-Squares Estimation of Nonlinear Parameters.
670 Journal of the Society for Industrial and Applied Mathematics, 11, 431–441.

671 Moy, A., and Fournelle, J. (2021) ϕ(ρz) Distributions in Bulk and Thin Film Samples for EPMA.
672 Part 1: A Modified ϕ(ρz) Distribution for Bulk Materials, Including Characteristic and
673 Bremsstrahlung Fluorescence. Microscopy and Microanalysis, 1–18.

674 Moy, A., Merlet, C., Llovet, X., and Dugne, O. (2013) Measurements of absolute L- and M-
675 subshell x-ray production cross sections of Pb by electron impact. Journal of Physics B:
676 Atomic, Molecular and Optical Physics, 46.

677 Moy, A., Fournelle, J., and von der Handt, A. (2019a) Quantitative Measurement of Iron-
678 Silicides by EPMA Using the Fe Lα and Lβ X-ray Lines: A New Twist to an Old Approach.
679 Microscopy and Microanalysis, 25, 664–674.

680 Moy, A., Fournelle, J.H., and von der Handt, A. (2019b) Solving the iron quantification problem
681 in low-kV EPMA: An essential step toward improved analytical spatial resolution in
682 electron probe microanalysis—Olivines. American Mineralogist, 104, 1131–1142.

683 Pinard, P.T., and Richter, S. (2014) Improving the quantification at high spatial resolution using a
684 field emission electron microprobe. IOP Conference Series: Materials Science and
685 Engineering, 55, 012016.

686 Pouchou, J.-L., and Pichoir, F. (1991) Quantitative analysis of homogeneous or stratified
687 microvolumes applying the model “PAP.” In K.F.J. Heinrich and D.E. Newbury, Eds.,
688 Electron Probe Quantitation pp. 31–75. Springer New York.

689 Salvat, F. (2019) PENELOPE 2018: A code system for Monte Carlo simulation of electron and
690 photon transport. OECD.

691 Saunders, K., Buse, B., Kilburn, M.R., Kearns, S., and Blundy, J. (2014) Nanoscale
692 characterisation of crystal zoning. Chemical Geology, 364, 20–32.

693 Schrader, D.L., and Zega, T.J. (2018) Pyrrhotite And Pentlandite in LL3 to LL6 Chondrites:
694 Determining Compositional And Microstructural Indicators of Formation Conditions. In
695 49th Lunar and Planetary Science Conference. The Woodlands, Texas.

696 Schrader, D.L., Connolly, H.C., Lauretta, D.S., Zega, T.J., Davidson, J., and Domanik, K.J.
697 (2015) The formation and alteration of the Renazzo-like carbonaceous chondrites III:
698 Toward understanding the genesis of ferromagnesian chondrules. Meteoritics and Planetary
699 Science, 50, 15–50.

700 Terauchi, M., Koike, M., Fukushima, K., and Kimura, A. (2010) Development of wavelength-
701 dispersive soft X-ray emission spectrometers for transmission electron microscopes–an
702 introduction of valence electron spectroscopy for transmission electron microscopy. Journal
703 of Electron Microscopy, 59, 251–261.

704 Zhang, J., Li, L., Gilbert, S., Liu, J.J., and Shi, W.S. (2014) LA-ICP-MS and EPMA studies on
705 the Fe-S-As minerals from the Jinlongshan gold deposit, Qinling Orogen, China:
706 Implications for ore-forming processes. Geological Journal, 49, 482–500.

707 Ziebold, T.O., and Ogilvie, R.E. (1963) Quantitative Analysis with the Electron Microanalyzer.
708 Analytical Chemistry, 35, 621–627.

709 Zschornack, G. (2007) Handbook of X-ray data, 1–969 p. Handbook of X-Ray Data. Springer
710 Berlin Heidelberg, Berlin, Heidelberg.

711

712 **Figure 1.** X-ray production volumes of the Fe Kα and Fe Lα lines in pyrite (FeS_2) at 7, 10 and 20
713 kV, obtained by Monte Carlo simulations using the PENEPMA/PENELOPE code (Llovet and
714 Salvat 2017; Salvat 2019). An electron beam diameter of 80 nm was used. The outer green contour
715 shows the limit within which 99% of the considered X-rays are produced.

716
717
718 **Figure 2.** Fe Lα and Fe Lβ X-ray lines measured on stannite, pyrite and Fe metal at 7 kV and 90
719 nA using WDS detectors to study the impact of carbon contamination. Spectra recorded by moving
720 the monochromator crystal from low-to-high or high-to-low energies are very similar, indicating
721 that the carbon contamination has limited impact on the measurements. The continuous grey line
722 at the bottom of each plot represents the intensity difference (in c/s/nA) between spectra measured
723 in opposite directions.

724
725 **Figure 3.** Fe concentration determined by the traditional quantification method, with either pure
726 Fe or pyrite as a standard, at 7 kV using the Fe Lα X-ray line versus the actual Fe concentration
727 (in wt%). Error bars are of the size of the symbols or smaller. The large deviations from the 1:1
728 diagonal indicate that the Fe Lα X-ray lines are not suitable for use with the traditional
729 quantification method.

730
731 **Figure 4.** Fe L spectrum measured on a pyrite standard at 7 kV and 90 nA. Panel (a) shows the L
732 lines of Fe. Panel (b) is a close-up of the spectrum on the Fe Lℓ and Lη X-ray lines. Symbols are
733 the experimental data, continuous lines are the pseudo-Voigt functions fitting the different X-ray
734 lines, dot dashed lines represent the background, and the dashed line is the sum of the fitting
735 functions.

736

737 **Figure 5.** Experimental Fe Lα+Lβ area k-ratios plotted as a function of the Fe concentration.
738 Panel (b) is a close-up of the lower Fe concentration Fe-sulfides. The area k-ratios for pyrite,
739 pyrrhotite and troilite are similar even though their Fe concentrations are different.

740

741 **Figure 6.** Spectra of the Fe Lα and Fe Lβ X-ray lines measured on pyrite, pyrrhotite and troilite
742 at 7 kV and 90 nA using a LTAP crystal. Despite containing less iron, pyrite has a more intense
743 Fe Lα X-ray line intensity than pyrrhotite and troilite.

744

745 **Figure 7.** Calibration curves obtained for (a) low Fe concentrations using the Fe Lα+Lβ area k-
746 ratio and (b) high Fe concentration using an average of the Fe Lα and Lβ area k-ratios (see text
747 for details). The area k-ratios were averaged between the different spectrometers and fitted with
748 polynomial functions.

749

750 **Figure 8.** Quantification of Fe in Fe-sulfide samples at 7 kV using the calibration curves. Three
751 different spectrometers were used to obtain area k-ratios. The X axis represents the measured Fe
752 concentration while the Y axis represents the known concentration. Results fall closely to the 1:1
753 line.

754

755 **Table 1.** Diameter of the X-ray interaction volume where 99% of the considered characteristic X-
756 rays are produced as a function of the accelerating voltage for the Fe Kα and Fe Lα X-ray lines.

X-ray line	7 kV	10 kV	20 kV
Fe Kα	–	1.10 μm	2.80 μm
Fe Lα	0.56 μm	0.99 μm	3.15 μm

757

758

This is the peer-reviewed, final accepted version for American Mineralogist, published by the Mineralogical Society of America.
The published version is subject to change. Cite as Authors (Year) Title. American Mineralogist, in press.
DOI: https://doi.org/10.2138/am-2022-8027. http://www.minsocam.org/

759 **Table 2.** Compositions of the iron-sulfide standards used in this study (in wt%). The Fe
760 compositions were measured at 15 kV (and 20 kV for the arsenopyrite standard) using the
761 traditional Kα line. (AMNH: American Museum of Natural History; MAC: Micro-Analysis
762 Consultants Ltd, England; NMNH: National Museum of Natural History)

Sample name	Fe	Zn	S	Sn	Co	Ni	Cu	As	Total	Source
Fe	100	–	–	–	–	–	–	–	100	
FeS (Czamanske4)	63.41±0.24	–	35.84±0.20	bdl	bdl	bdl	–	bdl	99.25±0.31	Czamanske collection
Canyon Diablo troilite	62.98±0.33	–	36.02±0.12	bdl	bdl	bdl	–	bdl	99.00±0.35	NMNH
FeS (Mnt 8)	62.97±0.20	–	36.04±0.11	bdl	bdl	bdl	–	bdl	99.01±0.22	AMNH
Pyrrhotite	60.41±0.17	bdl	39.51±0.11	bdl	–	–	–	–	99.92±0.21	MAC
Pyrite	46.73±0.23	bdl	53.48±0.17	bdl	–	–	–	–	100.21±0.28	MAC
Arsenopyrite	34.32±0.14	–	18.02±0.27	–	bdl	bdl	–	48.33±0.21	100.67±0.37	MAC
Pentlandite	30.62±0.22	0.16±0.04	33.34±0.09	bdl	0.83±0.11	35.30±0.15	–	–	100.25±0.30	MAC
Chalcopyrite	30.29±0.16	bdl	34.72±0.12	bdl	bdl	–	34.28±0.24	–	99.29±0.31	MAC
ZnFeS (Czamanske37)	23.16±0.21	42.00±0.46	33.64±0.30	–	–	–	–	–	98.80±0.59	Czamanske collection
Stannite	11.68±0.14	1.46±0.17	29.33±0.05	18.87±0.22	bdl	–	38.86±0.15	–	100.20±0.35	MAC
Bornite	11.37±0.24	bdl	25.76±0.14	bdl	bdl	–	62.85±0.65	–	99.98±0.70	MAC
Cobaltite	9.40±0.21	–	19.95±0.13	bdl	17.15±1.05	9.87±0.69	–	42.95±1.07	99.32±1.67	MAC
ZnFeS (Czamanske35)	5.62±0.08	60.74±0.60	32.59±0.12	–	–	–	–	–	98.95±0.62	Czamanske collection
Chalcocite	0.44±0.08	–	20.16±0.2	–	–	–	79.4±0.8	–	100.0±0.83	MAC

763 bdl: below detection limit

764 –: not measured

765

This is the peer-reviewed, final accepted version for American Mineralogist, published by the Mineralogical Society of America.
The published version is subject to change. Cite as Authors (Year) Title. American Mineralogist, in press.
DOI: https://doi.org/10.2138/am-2022-8027. http://www.minsocam.org/

766 **Table 3.** Quantification of the Fe-sulfide samples using the Fe Lℓ X-ray line with two different
767 analysis software: Probe for EPMA and BadgerFilm (see text for details). Expected concentration
768 as well as the relative error are also given.

Sample name	Probe for EPMA			BadgerFilm	
	Fe wt% (Kα line, 15 kV)	Fe wt% (Lℓ line, 7 kV)	Rel. Err. (%)	Fe wt% (Lℓ line, 7 kV)	Rel. Err. (%)
FeS (Czamanske4)	63.41±0.24	62.40	-1.60	64.12	1.12
Canyon Diablo troilite	62.98±0.33	62.76	-0.35	63.95	1.54
FeS (Mnt 8)	62.97±0.20	62.96	-0.02	63.94	1.54
Pyrrhotite	60.41±0.17	59.68	-1.20	60.47	0.10
Pyrite	46.73±0.23	45.87	-1.84	46.50	-0.49
Arsenopyrite	34.32±0.14	32.79	-4.45	33.01	-3.82
Pentlandite	30.62±0.22	30.85	0.76	30.42	-0.65
Chalcopyrite	30.29±0.16	30.01	-0.93	30.90	2.01
Stannite	11.68±0.14	11.36	-2.77	11.30	-3.25
Bornite	11.37±0.24	11.23	-1.25	11.30	-0.62
Cobaltite	9.40±0.21	8.86	-5.72	9.41	0.11

769

This is the peer-reviewed, final accepted version for American Mineralogist, published by the Mineralogical Society of America.
The published version is subject to change. Cite as Authors (Year) Title. American Mineralogist, in press.
DOI: https://doi.org/10.2138/am-2022-8027. http://www.minsocam.org/

770 **Table 4.** Fe concentration (wt%) obtained using the area k-ratio calibration curve at 7 kV with
771 the CAMECA SX51 instrument and with three different WDSs.

Sample name	Nominal Fe wt%	SX51, Sp1 TAP	SX51, Sp2 TAP	SX51, Sp4 PC0
FeS (Czamanske4)	63.41	65.28	-	63.75
Canyon Diablo troilite	62.98	60.89	65.02	62.28
FeS (Mnt 8)	62.94	61.28	62.92	62.27
Pyrrhotite	60.41	62.83	63.60	60.37
Pyrite	46.73	48.17	47.76	49.05
Pentlandite	30.62	31.63	30.14	28.84
Chalcopyrite	30.29	29.90	29.92	30.08
ZnFeS (Czamanske37)	23.16	20.87	19.34	20.05
Stannite	11.68	9.50	9.82	10.56
Bornite	11.37	11.82	11.97	11.74
Cobaltite	9.4	8.16	9.06	9.16
ZnFeS (Czamanske35)	5.62	6.56	-	5.42

772

773

This is the peer-reviewed, final accepted version for American Mineralogist, published by the Mineralogical Society of America.
The published version is subject to change. Cite as Authors (Year) Title. American Mineralogist, in press.
DOI: https://doi.org/10.2138/am-2022-8027. http://www.minsocam.org/

774 **Table 5.** Comparison of the Fe quantification results (in wt%) obtained using the traditional method
775 with the Fe Lα X-ray intensity and using the area k-ratio calibration curve method on the CAMECA
776 SX51 instrument. The relative error, relative to the nominal Fe concentration, is also indicated.

Sample name	Nominal Fe wt%	Traditional method	Rel. Err. (%)	Calibration curve	Rel. Err. (%)
FeS (Czamanske4)	63.41	47.74	-24.7	65.28	3.0
Canyon Diablo troilite	62.98	46.88	-25.6	60.89	-3.3
FeS (Mnt 8)	62.94	47.33	-24.8	61.28	-2.6
Pyrrhotite	60.41	47.53	-21.3	62.83	4.0
Pyrite	46.73	65.48	40.1	48.17	3.1
Pentlandite	30.62	33.52	9.5	31.63	3.3
Chalcopyrite	30.29	27.26	-10.0	29.90	-1.3
ZnFeS (Czamanske37)	23.16	20.76	-10.3	20.87	-9.9
Stannite	11.68	12.66	8.3	9.50	-18.7
Bornite	11.37	12.43	9.3	11.82	4.0
Cobaltite	9.4	14.12	50.2	8.16	-13.2
ZnFeS (Czamanske35)	5.62	6.73	19.8	6.56	17.1

777

778

779 **Table 6.** Nominal composition, in wt%, of the unknown samples determined at 15 kV using the
780 traditional Kα X-ray lines.

Sample name	S	Fe	Cu	Total
Pyrrhotite	38.85±0.15	60.88±0.19	bdl	99.73±0.24
Chalcopyrite	34.96±0.14	30.20±0.09	34.35±0.12	99.51±0.21
Bornite	25.77±0.09	10.95±0.05	62.69±0.18	99.41±0.21

781 bdl: below detection limit.

782

783 **Table 7.** Quantification of Fe at 7 kV using the traditional method with the Fe Lα X-ray line, using
784 the area k-ratio calibration curves and using the traditional method with the Fe Lℓ line. Pure Fe
785 was used as a standard for all the methods. Concentrations are given in wt%.

786

Sample name	Nominal	Traditional method with the Lα X-ray line		Area k-ratio calibration curves		Traditional method with the Lℓ X-ray line CalcZAF		Traditional method with the Lℓ X-ray line BadgerFilm	
		LTAP	PC0	LTAP	PC0	LTAP	PC0	LTAP	PC0
Pyrrhotite	60.88	46.94	52.39	63.61	58.06	61.19	62.51	61.33	62.84
Chalcopyrite	30.20	28.07	32.45	30.93	30.85	31.19	31.42	31.24	31.47
Bornite	10.95	7.94	7.72	7.51	6.67	10.74	10.8	10.71	10.78

787

DOI: https://doi.org/10.2138/am-2022-8027. http://www.minsocam.org/

Figure 1

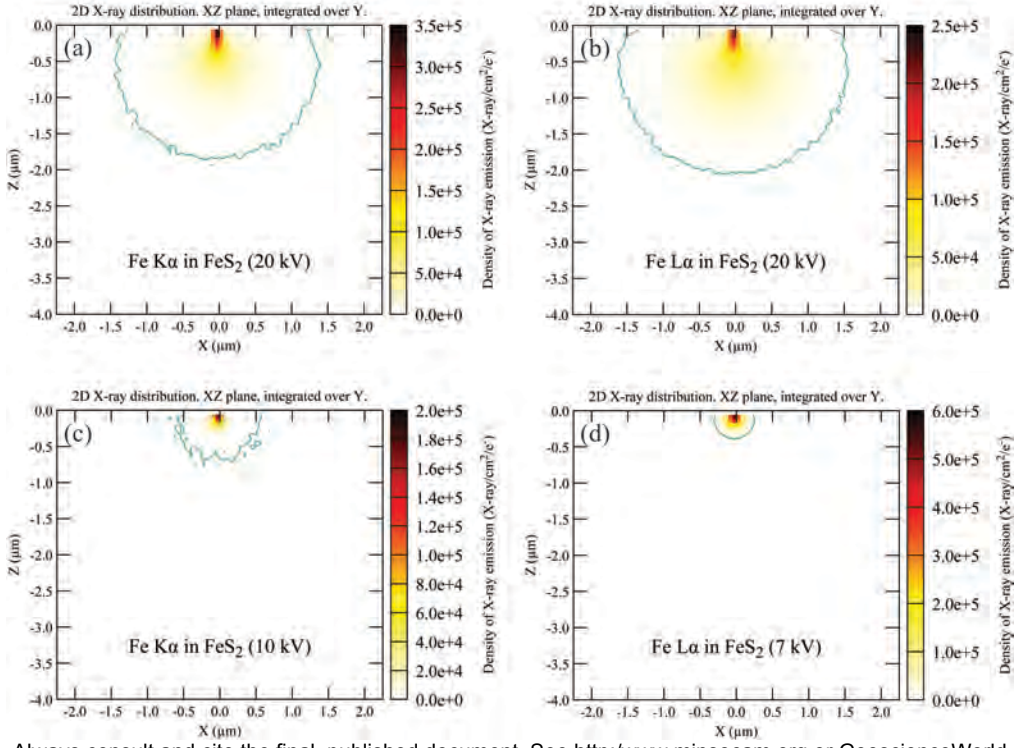

This is the peer-reviewed, final accepted version for American Mineralogist, published by the Mineralogical Society of America.
The published version is subject to change. Cite as Authors (Year) Title. American Mineralogist, in press.
DOI: https://doi.org/10.2138/am-2022-8027. http://www.minsocam.org/

Figure 2

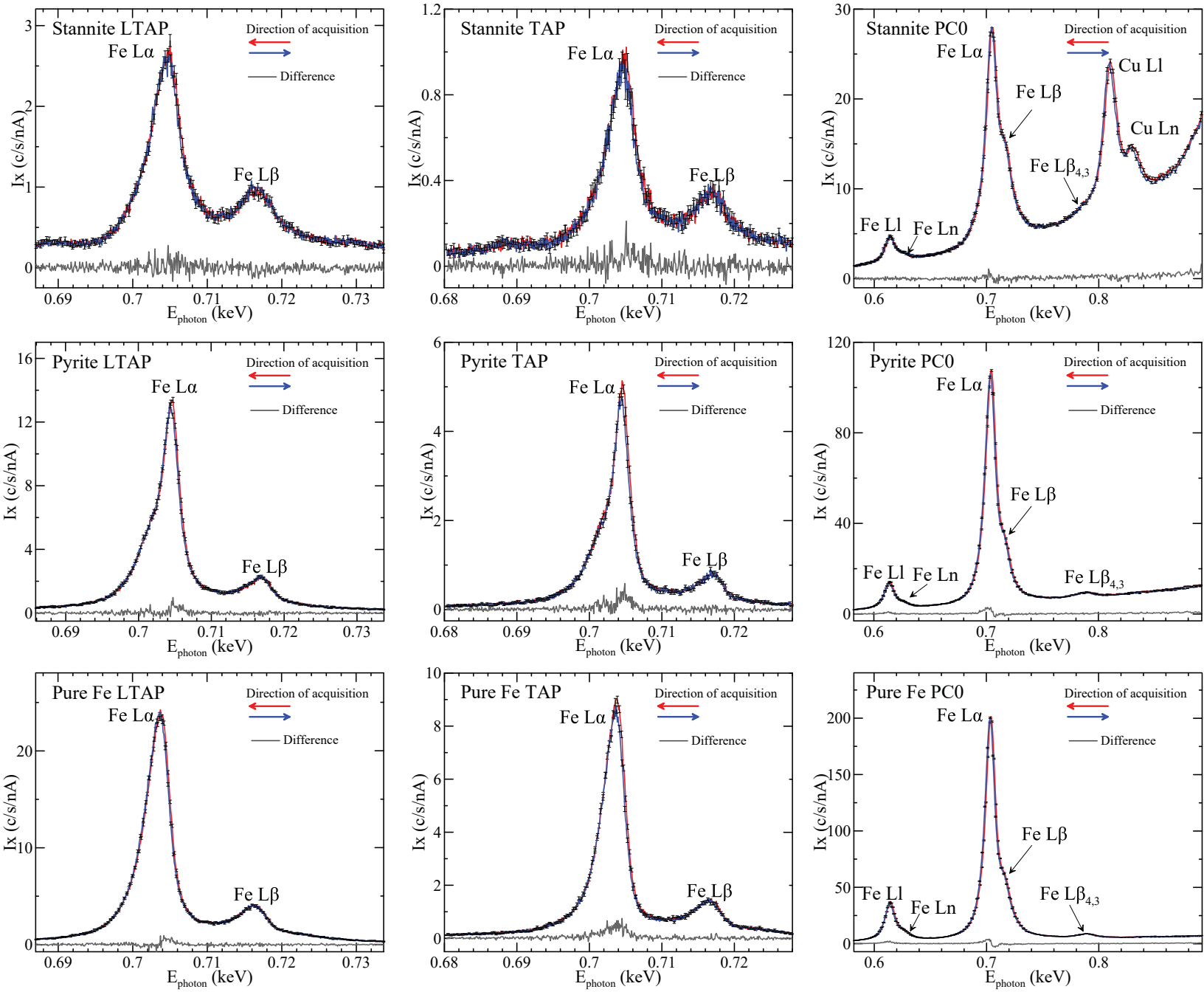

This is the peer-reviewed, final accepted version for American Mineralogist, published by the Mineralogical Society of America.
The published version is subject to change. Cite as Authors (Year) Title. American Mineralogist, in press.
DOI: https://doi.org/10.2138/am-2022-8027. http://www.minsocam.org/

Figure 3

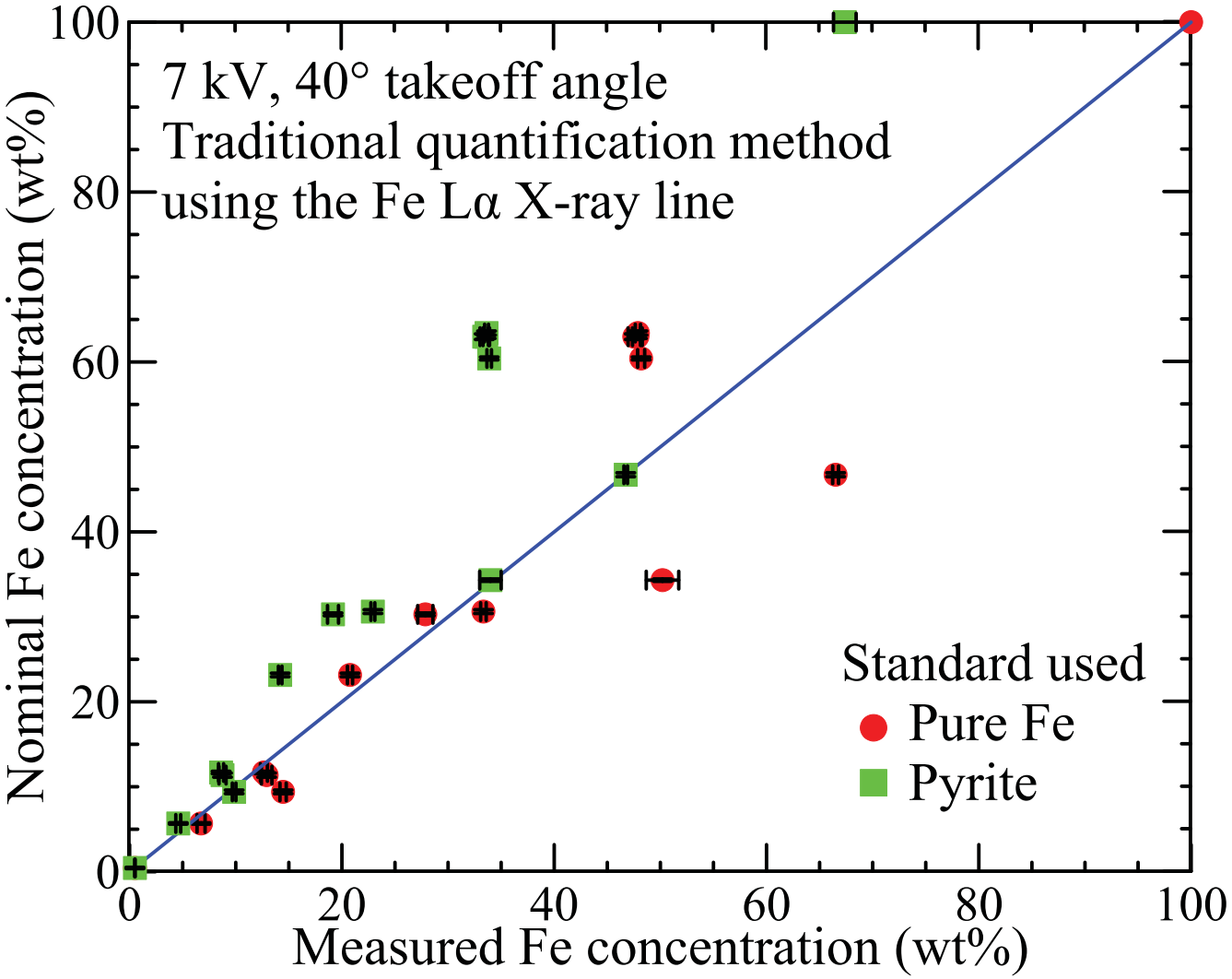

This is the peer-reviewed, final accepted version for American Mineralogist, published by the Mineralogical Society of America.
The published version is subject to change. Cite as Authors (Year) Title. American Mineralogist, in press.
DOI: https://doi.org/10.2138/am-2022-8027. http://www.minsocam.org/

Figure 4

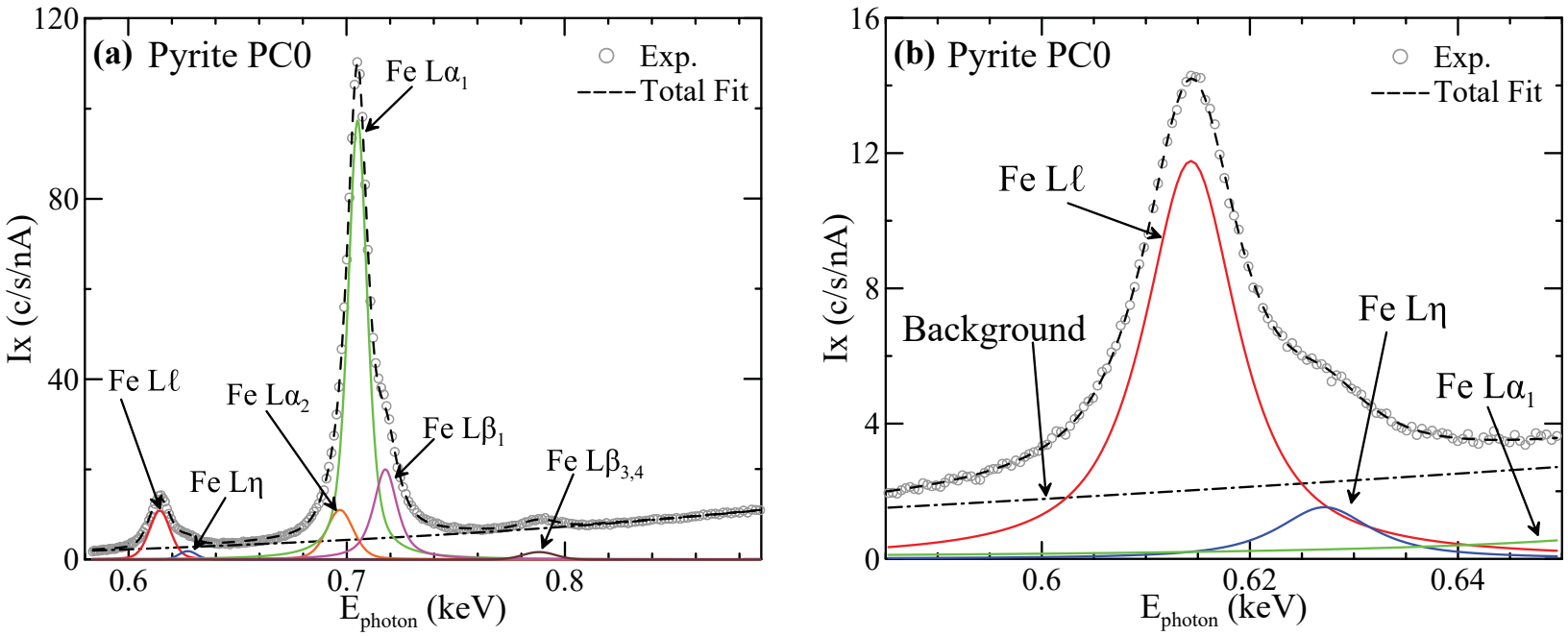

This is the peer-reviewed, final accepted version for American Mineralogist, published by the Mineralogical Society of America.
The published version is subject to change. Cite as Authors (Year) Title. American Mineralogist, in press.
DOI: https://doi.org/10.2138/am-2022-8027. http://www.minsocam.org/

Figure 5

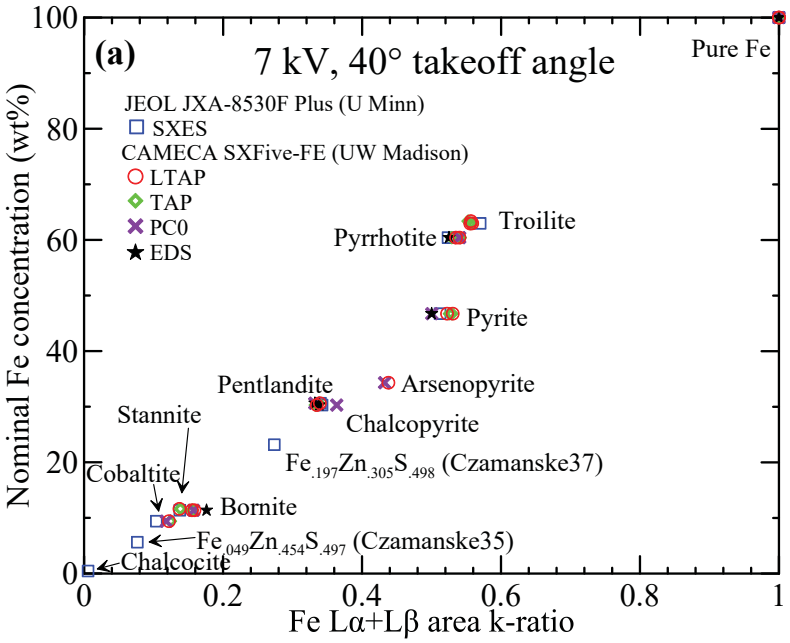

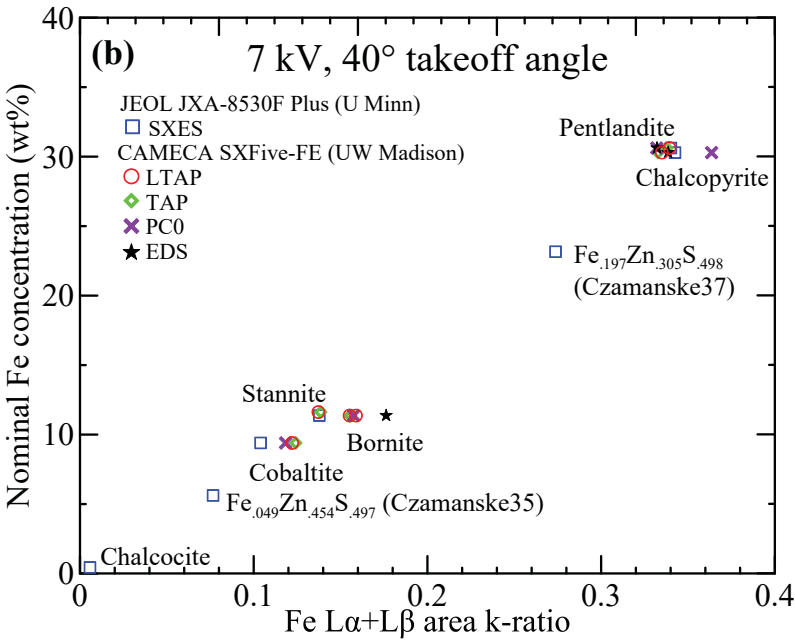

This is the peer-reviewed, final accepted version for American Mineralogist, published by the Mineralogical Society of America.
The published version is subject to change. Cite as Authors (Year) Title. American Mineralogist, in press.
DOI: https://doi.org/10.2138/am-2022-8027. http://www.minsocam.org/

Figure 6

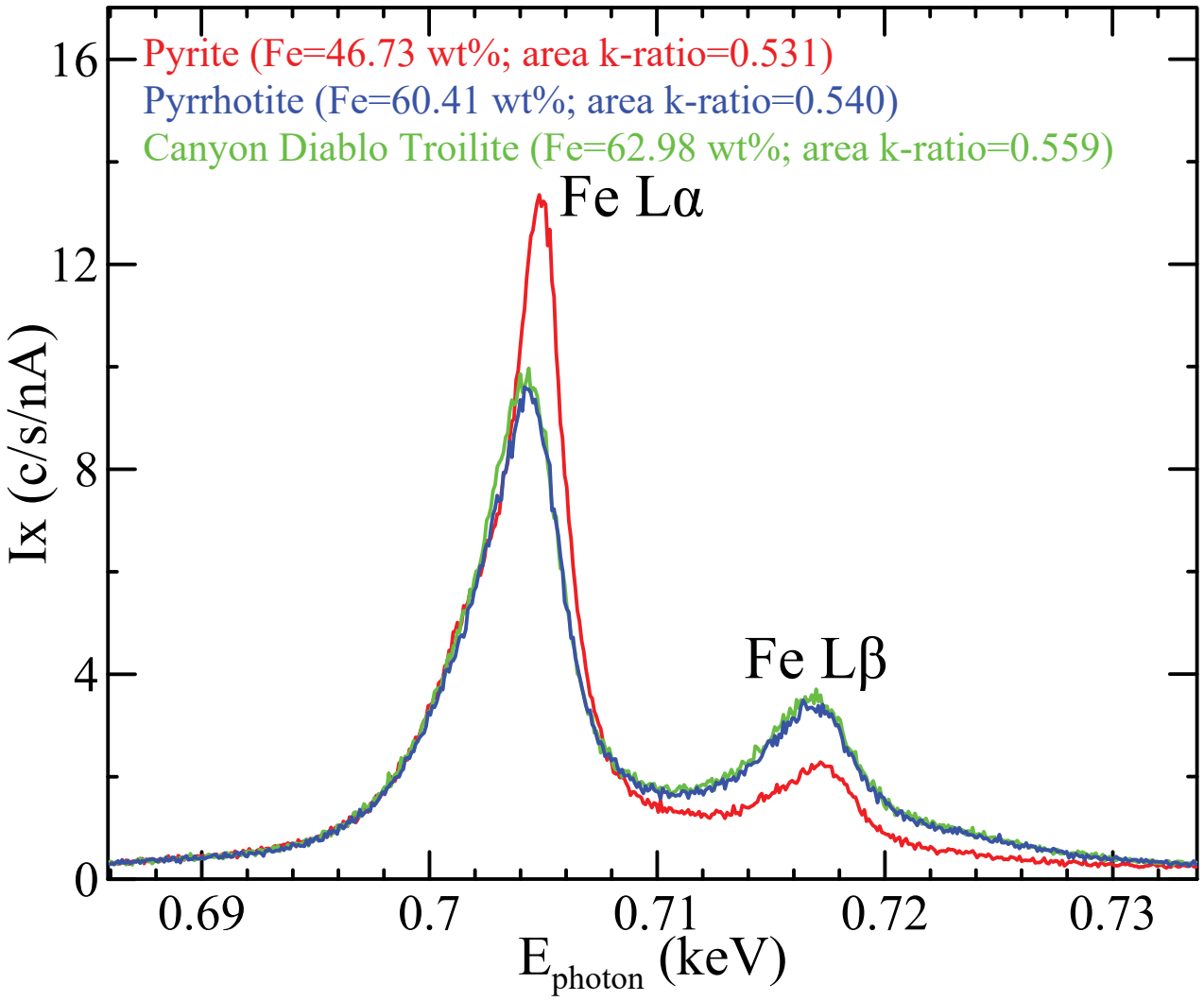

This is the peer-reviewed, final accepted version for American Mineralogist, published by the Mineralogical Society of America.
The published version is subject to change. Cite as Authors (Year) Title. American Mineralogist, in press.
DOI: https://doi.org/10.2138/am-2022-8027. http://www.minsocam.org/

Figure 7

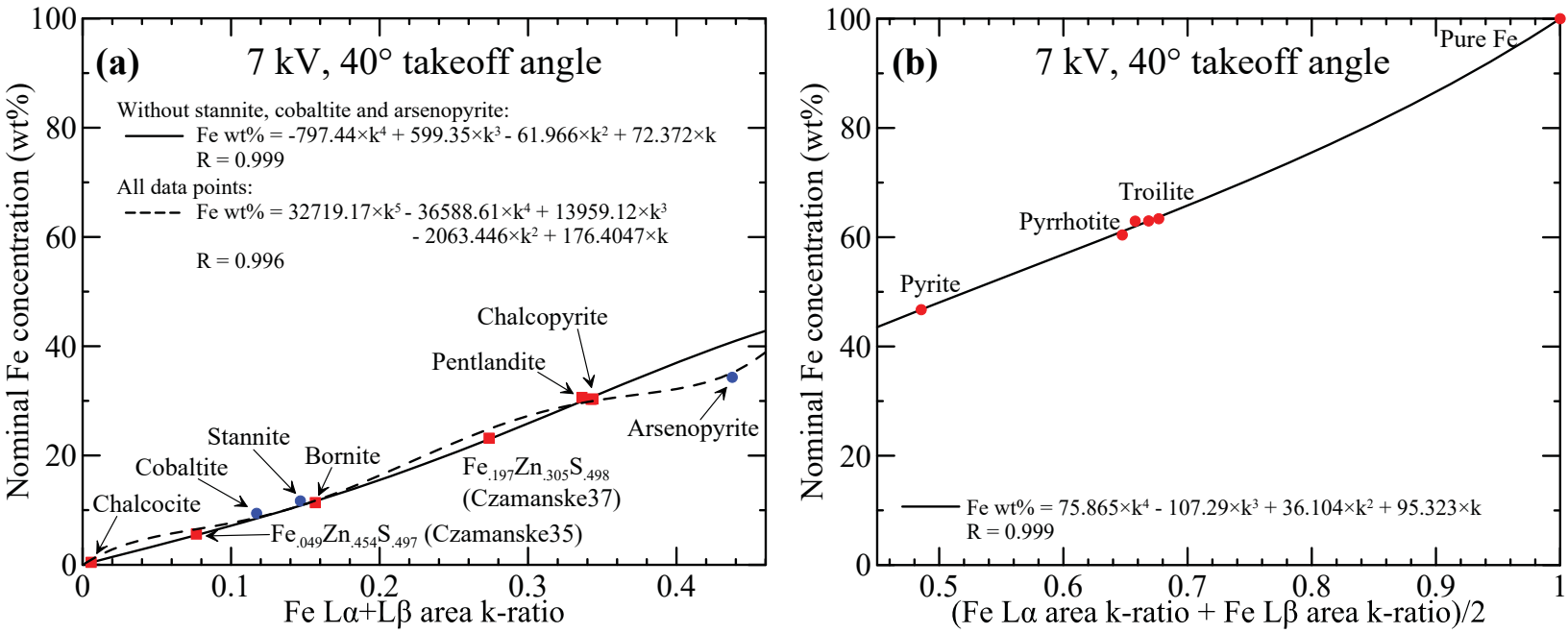

This is the peer-reviewed, final accepted version for American Mineralogist, published by the Mineralogical Society of America.
The published version is subject to change. Cite as Authors (Year) Title. American Mineralogist, in press.
DOI: https://doi.org/10.2138/am-2022-8027. http://www.minsocam.org/

Figure 8